

The Art of Staying Cool: Air Cooling for the Barrel DIRC Detector at $\bar{\text{P}}\text{ANDA}$

Guilherme Garcia

University of Edinburgh, guilhermeluis.garcia@gmail.com

Niclas Schilling

Eberhard Karls Universität Tübingen, niclas.schilling@student.uni-tuebingen.de

This project explored the potential of using compressed air to cool the Barrel DIRC detector at the $\bar{\text{P}}\text{ANDA}$ experiment, as well as the effects of higher temperatures on the detector's timing accuracy and dark count rate. While airflow rates of 80 to 100 l/min remove a significant amount of heat from the experimental setup with eight DiRICH boards, approximately 30 % of the energy is not transported away, potentially increasing the temperature equilibrium with other subdetectors. Higher temperatures negatively impact the timing accuracy of the detector, however, the accuracy seems to increasingly stabilize below temperatures of 50°C to 55°C. The dark count rate of the detector remains unaffected by temperature changes within the observed range of $\Delta T = 7^\circ\text{C}$. Further studies are necessary to optimize the airflow or explore additional cooling methods to ensure reliable performance.

1 Introduction

The $\bar{\text{P}}\text{ANDA}$ experiment (antiProton ANnihilation at DArmstadt) will be one of the four scientific pillars of FAIR (Facility for Antiproton and Ion Research in Europe). It will collide anti-protons with momenta in the range of 1.5 to 15 GeV/c with a fixed target in order to study strong interaction phenomena [1].

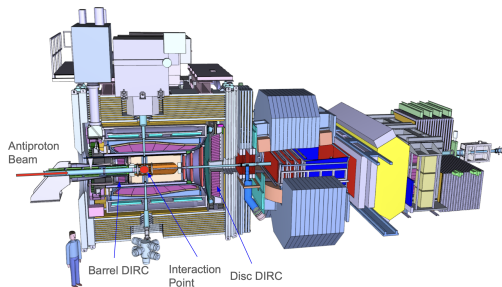


Fig. 1: $\bar{\text{P}}\text{ANDA}$ Detector [2]

1.1 The $\bar{\text{P}}\text{ANDA}$ DIRC detector

The detector will require fast and accurate Particle Identification (PID). PID for charged hadrons will mostly be done by two DIRC (Detection of Internally Reflected Cherenkov light) detectors, the Endcap Disk DIRC (that covers

angles between 2 and 22°) and the Barrel DIRC (that covers angles between 22 and 140° and which will be the focus of this report) [3] [4].

The photon detection is done by a Microchannel Plate Photomultiplier Tube (MCP-PMT) that is read out by the electronics board, the DiRICH System [1]. A DiRICH is composed of 32 amplifiers, one for each channel of the detector (each detector has 64 channels, so each detector is connected to 2 DiRICHs) and an FPGA (Field Programmable Gate Array) that provides the discriminator for the data.

The timing accuracy of the MCP-PMT - DiRICH system is about 100 ps. However, the heating of the system might cause extra noise in the electronic system of the DiRICH, which can affect its timing accuracy. As such it becomes essential not only to study ways to cool this system but also to study what kind of effect will the heating of the system have on the timing accuracy of the detector.

The main goals of this project are to test if it is possible to effectively cool the Barrel DIRC detector system with compressed air and if so, what kind of flow will be necessary to achieve that, how the temperature affects the timing accuracy of the measurements and what parts of this system are affected by the change in temperature.

2 Methodologies

2.1 Experimental Setup

To measure the behaviour of the DiRICHs and their timing accuracy at different temperatures, a wall was placed in the middle of an optical plate. On one side of the partition, three Photonis XP85012/A1-Q MCP-PMTs [5] and a light pulser (to allow for timing accuracy measurements) were mounted onto a circuit board, which was on the other side directly connected to eight DiRICHs (as seen in Fig. 2).

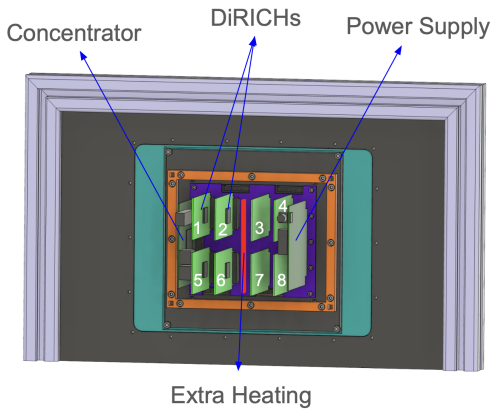


Fig. 2: Experimental Setup - Electronics view. In addition to the eight DiRICHs, the board also contains a concentrator and a power supply as well as additional heating in the center (red). The eight DiRICHs are numbered, in the same way as they are referred to in the following plots

A closed box was placed around the system, isolating it, except for the places that allow for the air to enter and leave the system and the entry for the light from the PiLas laser [6], which in turn was connected to a 50kHz pulser that acted as a trigger. To simulate the heating of a system with 4 detectors, an additional heating of 4W was added to the electronics box to simulate the power consumption by the high voltage divider, which wasn't included in the version of the hardware used for this experiment. The box was also equipped with Dallas DS18B20 temperature sensors to read the temperature of the incoming air, the temperature of the outgoing air and the temperature close to the surface of the MCP-PMTs (see Fig. 3). These were connected through a Raspberry Pi server to the lab network allowing for easy access to this data. The required airflow through the closed box could be

adjusted to the desired rate using a compressed air regulator (with a range between 20 and 100 l/min), which was connected in front of the air inlet to the box.

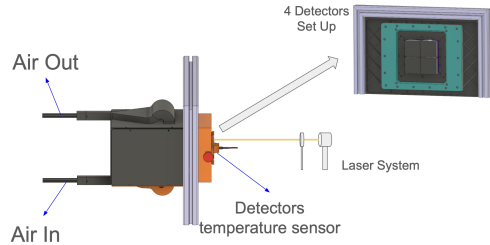


Fig. 3: Experimental Setup - External view

The setup allowed for the quantification of the airflow as well as the accurate measurement of the incoming and outgoing air temperature of the system, which made it possible to measure the power that was removed from the system through air circulation (see also chapter 2.3).

A picture of the laboratory setup is shown in Fig. 4. On the left side, the mentioned box can be seen, which is normally closed by the black lid with the air outlet shown behind. For the recording of the outgoing air temperature a sensor is hidden in the air outlet. Inside the box, from front to back, the power supply, two DiRICHs, the external heater (plastic partition and circuit board), two more DiRICHs and the data concentrator can be recognized. On the right side, the laser (yellow cable) is pointed at a diffuser, from where the laser light can then enter the orange box through a hole in the front. This smaller box covers the MCP-PMT detectors and another temperature sensor (indicated by the orange, red cable entering the housing).



Fig. 4: Picture of the measurement setup used

2.2 Data Acquisition

While the temperatures for incoming and outgoing air as well as the detector temperature were measured by externally mounted sensors (see Fig. 3), DS18B20 temperature sensors were already pre-installed on the DiRICHs. A thermal camera image of the board in Fig. 5 shows that the main heat source of the DiRICHs are the FPGA chips (in the image below at a temperature around 50°C). The DiRICHs integrated thermal sensors are located at a certain distance from the FPGAs and thus provide a lower bound for the temperature of the electronics. Furthermore in order to dissipate the heat more effectively, cooling fins were applied to the FPGAs.

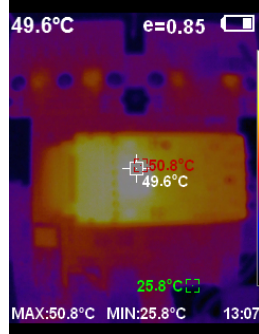


Fig. 5: Thermal image of DiRICH with the FPGA at the center and the less warm circuit board around it

The setup and the mentioned temperature sensors were used to record the temperature curves of the eight DiRICHs and the three sensors (In, Out and Detectors, see Fig. 3) at different air flow rates between 20 and 100 l/min. A typical such curve is shown in Fig. 6, here for a flow rate of 90 l/min.

As can be seen, equilibrium was reached after approximately 80 minutes, the exact length of the period depends on the flow rate. For the discussion of the non-negligible temperature differences between the different DiRICHs see chapter 3.1.

2.3 Heat Transport

Assuming that all the outgoing air has reached the temperature measured by the corresponding temperature sensor, the cooling capacity $P_{air} = \dot{Q}_{air}$, i.e. the heat removed by air in a certain time, was calculated. Assuming room condition values (temperature of 23 °C, relative

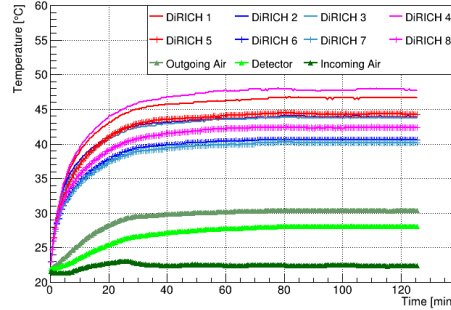


Fig. 6: Temperature curves of the eight DiRICHs (numbered from 1 to 8) as well as for the incoming air, outgoing air and detector sensors at a flow rate of 90 l/min

humidity of 40.85% and pressure of 101325 Pa) for the density $\rho = 1.187 \text{ kg m}^{-3}$ and the isobaric heat capacity $c_p = 1.012 \text{ J g}^{-1} \text{ K}^{-1}$ of air, the following formula can be obtained:

$$P_{air}[\text{W}] = 0.020 \frac{\text{min}}{1 \cdot \text{K}} \text{W} \cdot \text{FlowRate} \cdot \Delta T \quad (1)$$

This indicates the thermal power removed at a given air flow rate and temperature difference ΔT between incoming and outgoing air. By applying Eq. 1 to the measurement in Fig. 6, the timing-dependent power transport out of the whole system was calculated as shown in Fig. 7

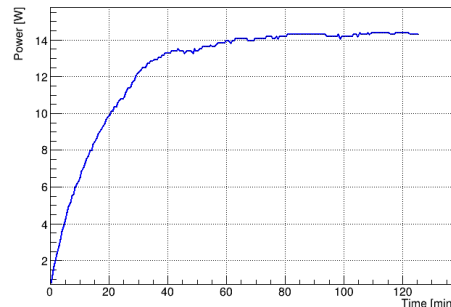


Fig. 7: Time-dependent power transported out of the system by air cooling at a flow rate of 90 l/min

2.4 Dark Counts

To understand the effect of temperature variations on timing accuracy, it is necessary to check whether or not the MCP-PMT was affected by an increase in temperature. This was done by measuring the detector's dark counts,

which occur because photoelectrons are emitted thermally even in the absence of irradiation. By comparing the dark count rates at different temperatures, it is possible to evaluate whether or not higher temperatures lead to an increase in noise.

This test was conducted by measuring the dark counts from 16 different pixels, with no laser incident on them for 20 seconds, and averaging the counts over their overall area. However, there's an extra factor that needs to be accounted for. Although the laser was not directed at the pixels, it still needed to be used as a trigger for the measurements. The laser emitted light at a frequency of 50 kHz (providing a trigger every 20 μ s), while the detector had a measurement interval of 1 μ s. This means that $\frac{19}{20}$ of the actual dark counts were missed in our measurements due to the detector's insensitivity during the remaining time. Therefore, the calculation for the dark counts (see Eq. 2) must average over the pixel area and measurement time, while also correcting for the missing counts due to the trigger limitation.

$$\text{Counts} \left[\frac{1}{\text{cm}^2 \cdot \text{s}} \right] = \text{Data} \cdot \frac{20}{0.36 \text{cm}^2 \cdot 16 \cdot 20 \text{s}} \quad (2)$$

2.5 Timing accuracy

To test the timing accuracy of the system, a Time over Threshold (ToT) technique was used. This determines the signal amplitude by using a discriminator. The longer the voltage of the signal is above a given threshold, the greater the amplitude of the signal will be. Similarly, if the amplitude of the signal doesn't reach the threshold, no output is released, which helps exclude part of the detector noise. Comparing the difference between the time arrival of different coinciding signals (signals with the same ToT) provides us with the strategy to analyse the timing accuracy of the system.

However, there are factors that can affect the resolution of the ToT technique, namely jitter and time walk effects. Jitter is caused by noise in both the detector and the electronics [7], causing fluctuations in the signals received, making it look like two different signals have crossed the threshold at the same time, even though they didn't. The time walk effect is caused by small fluctuations in the amplitude of the signal produced by the laser, since smaller

signals will overcome the discriminator threshold later than larger ones, this will affect the ToT results.

To quantify the uncertainty on time, the pulser, which worked as the trigger for our laser (with an amplitude of 40 mV and a high signal-to-noise ratio), was connected to two of the DiRICH's channels. Firstly, to prevent the effects of the time walk, a fixed amplitude of the signal was selected by applying a sharp ToT selection around its maximum ($|ToT - ToT_{maximum}| < 0.1ns$). Once this region has been determined, the timing accuracy of the system can be calculated by computing the standard deviation of the difference between the arrival time of the laser and the trigger signals, as shown in Fig. 8.

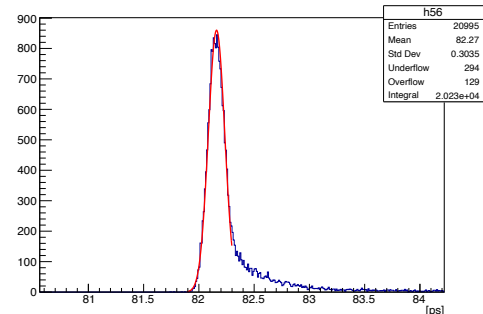


Fig. 8: Example of a best-fit calculation to determine the timing accuracy of the system. In this case, the test was done for a 20 l/min run with the result being $\sigma = 70.9(4)\text{ps}$, by using a Gaussian fit in range that avoided the tail of the distribution.

Furthermore, since the aim is to calculate the error of the pixel channel and not of the combination of the pixel and trigger channels, the error between the two pulser inputs was subtracted from the previously calculated timing accuracy. Thus obtaining the true timing accuracy of the MCP-PMT - DiRICH system (see Eq. 3).

$$\sigma = \sqrt{\sigma_{\text{system}}^2 - \sigma_{\text{pulser}}^2} \quad (3)$$

3 Results and Discussion

Our results can be divided into several partial measurements and findings. In the final PANDA detector, there is only limited space available to mount air pipes for cooling pur-

poses. Accordingly, the critical factor determining the feasibility of air cooling is the flow rate of air required to cool the detector. An interesting parameter is therefore the final temperature of the DiRICHs at different flow rates, which is analyzed in section 3.1. In the subsequent chapter 3.2, the composition of the equilibrium between incoming and outgoing power, which is established at these final temperatures, is investigated. To understand the upper-temperature limit for the experimental setup, the timing accuracy of the DiRICHs and the dark count rate of the MCP-PMTs at different temperatures are discussed in the chapters 3.3 and 3.4.

3.1 Equilibrium Temperatures

Fig. 9 shows the final temperatures of all eight DiRICHs, after equilibrium has been reached in the system, plotted against different flow rates.

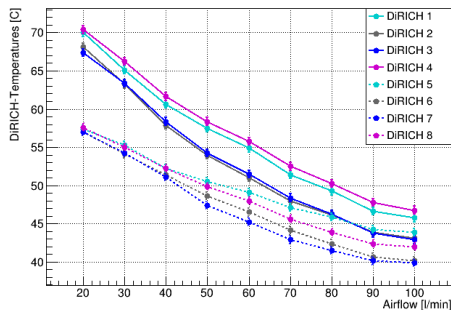


Fig. 9: Equilibrium temperatures for all eight DiRICHs at flow rates between 20 and 100 l/min

As expected, a clear anti-correlation between the flow rate and the temperatures is visible. For smaller flow rates the temperature increase when decreasing the rate by a certain amount is more dramatic compared to larger flow rates. As seen in Fig. 6, the final temperatures show large differences between the single DiRICHs across all flow rates. These variations can be reconciled with the spatial arrangement of the DiRICHs within the closed box sketched in Fig. 2. Especially at low flow rates, the four DiRICHs located in the lower half (from 5 to 8, sketched with dashed lines) are significantly better cooled than the upper four DiRICHs (from 1 to 4, sketched with full lines). The lower DiRICHs benefit from their proximity to the air intake and the advantageous position regarding the temperature gradient within the box. In par-

ticular, the DiRICH positions in the upper two corners of the box (1 and 4) appear to lead to unfavourable heat accumulation and thus higher temperatures.

Additional factors affecting the final temperature are given by the distance to the additional heating in the middle, to the power supply and to the concentrator, which are located respectively to the right and to the left of the DiRICHs (for a sketch of the relative DiRICH positions, see Fig. 2). It should be mentioned that occasional electronic failures have already occurred at the lowest flow rates tested, which is why lower rates were not considered. It appears, that for the highest measured temperatures, the maximum tolerable temperature has already been exceeded for at least some of the components.

Besides the final temperatures of the DiRICHs, the temperatures of the sensor near the MCP-PMT detectors and for the incoming and outgoing air can be plotted, as shown in Fig. 10. Similarly to the DiRICHs, the temperature of the detector is flow rate dependent, but significantly lower than the temperature of the DiRICHs at the same rate. However, it should be noted that in the context of a well-insulated system such as the PANDA detector, a new equilibrium with higher final temperatures could possibly develop over a period of days or weeks.

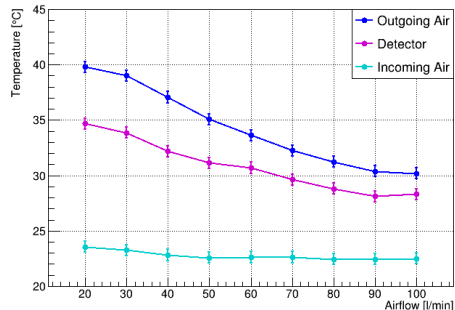


Fig. 10: Equilibrium temperatures for the detector sensor, incoming and outgoing air at different flow rates.

3.2 Heat Transport

Based on the plots of the air cooling capacity over time, as illustrated in Fig. 7, the mean equilibrium values can be plotted against the air

flow rate. Moreover, due to changing temperatures for different flow rates, the power itself, which is dissipated by the electronics, changes over the spectrum of temperatures reached at different rates. Both parameters are displayed in Fig. 11.

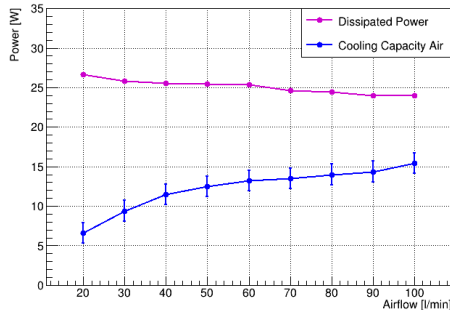


Fig. 11: Dissipated power by electronics in the studied system (purple) and heat transported out through air (blue). The purple error bars are smaller than the symbols used.

While the heat P_{air} , which can be removed by air cooling, increases significantly at higher flow rates, the total power input into the system P_{tot} falls slightly due to the decreasing temperature at higher rates. These two effects together cause the efficiency, calculated by the proportion of the heat output removed to the total power dissipated

$$\text{Efficiency}[\%] = \frac{P_{air}}{P_{tot}} \cdot 100 , \quad (4)$$

to increase significantly at higher air flows, as shown in Fig. 12.

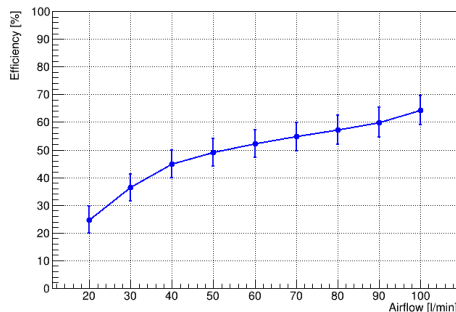


Fig. 12: Efficiency for cooling the DiRICHs with air at different flow rates

Given that the measurements for these graphs

were taken in a state of approximate equilibrium, it can be inferred that, even at 100 l/min, approximately 35% of the heat input into the system is released to the environment through pathways other than the intended airflow. These effects are mainly thermal radiation and heat conduction to the environment (optical table, etc.).

3.3 Timing accuracy

As shown in Fig. 13 and Fig. 14, there is a clear dependence of the timing accuracy in terms of temperature, however for lower temperatures this seems to stabilise and fluctuate around similar values. Thus for flow levels above 50 l/min the timing accuracy of the detector seems to be stable. This means that, for high flow rates, the main factor determining whether or not a given flow rate is adequately cooling the system will be the total power removed, since the timing accuracy will have stabilized at that stage. The changing values outside of the determined error bars indicate a missing systematic error in the measurements in the other of 2 ps.

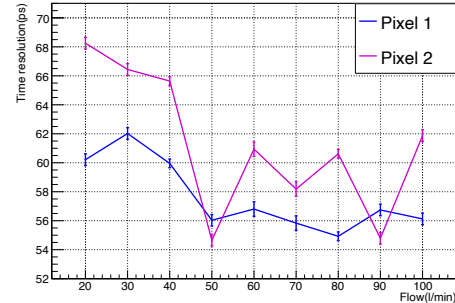


Fig. 13: Timing accuracy in terms of airflow

3.4 Dark-Counts

The dark counts of the detector show no dependence on the temperature consistently remaining within 100 counts/cm²s, as illustrated in Fig. 15 and Fig. 16. This can also be caused by the fact that, despite efforts to increase airflow towards the detectors warming them up, their temperatures never varied significantly enough to allow us visualizing any changes in the dark counts (see Fig. 10). However, the data does not suggest any clear trend or correlation be-

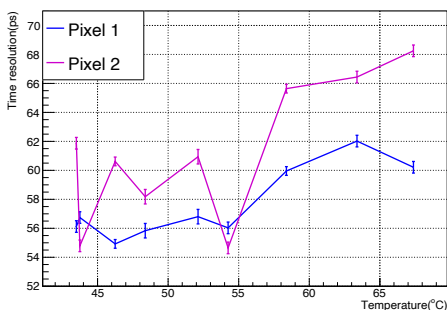


Fig. 14: Timing accuracy in terms of the temperature of the DiRICH reading the pixel information.

tween temperature and dark count rates in the examined temperature range.

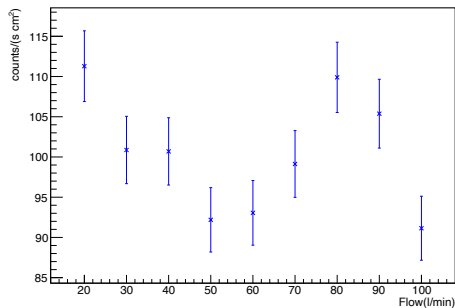


Fig. 15: Dark counts as a function of airflow

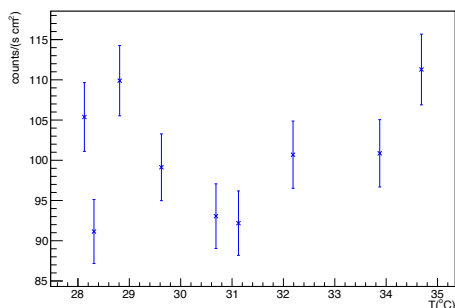


Fig. 16: Dark Counts in terms of the temperature of the detector.

4 Conclusion

This study has made progress in understanding and quantifying the cooling needs of the Barrel

DIRC detector. The current air cooling setup has shown effectiveness, especially at higher airflow rates, but it still falls short of ensuring reliable operation under all conditions. Despite the improvements in cooling efficiency, a significant amount of heat is still being radiated away.

In terms of the temperature's effect on the system, the increase does not impact the MCP-PMTs in the examined range, as the dark count rate remains stable. However, higher temperatures negatively affect the timing accuracy of the entire system. To maintain optimal performance and avoid timing degradation, we recommend not to exceed operating temperature ranges of 50°C to 55°C.

To build on these results, further research is necessary. One area of focus should be directing airflow more precisely onto the FPGA chips on the DiRICH boards, which are primary sources of heat. Additionally, investigating the effects of pre-cooling the air before it enters the detector could further reduce system temperatures. If air cooling proves insufficient, alternative methods like liquid cooling should be considered to optimize thermal management.

In summary, while we've achieved a better understanding of the cooling requirements and improved the quantification of heat management, the air cooling strategy needs further refinement. Future efforts should focus on optimizing the cooling setup to keep all components within safe temperature limits, ensuring optimal detector performance.

5 Acknowledgements

We would like to express our sincere gratitude to our supervisor Dr. Carsten Schwarz for his invaluable guidance and support throughout this project. His patience and willingness to explain complex concepts - along with the fascinating insights into the world of amateur radio - created a summer that was both enjoyable and rich in learning. We would also like to thank Dipl.-Ing. Andreas Gerhardt for designing the baseline experimental setup we used, for his assistance in assembling it, and for kindly allowing us to use his CAD designs in this report. Furthermore, we are deeply grateful to Dr. Ralf Averbeck for his key role in organizing the summer program and his ongoing support during our stay.

References

- [1] ETZELMÜLLER, E., ET AL. The PANDA DIRC detectors. *Nuclear Instruments and Methods in Physics Research Section A: Accelerators, Spectrometers, Detectors and Associated Equipment* 952 (2020), 161790. DOI: 10.1016/j.nima.2019.01.017.
- [2] BELIAS, A. Overview of the PANDA detector design at FAIR. *International Journal of Modern Physics: Conference Series* 51 (2023), 2360001. DOI: 10.1142/S2010194523600017.
- [3] COLLABORATION, T. P. PANDA Technical Design Report - Endcap Disc DIRC. arXiv: 1912.12638.
- [4] COLLABORATION, T. P. Technical Design Report for the PANDA Barrel DIRC Detector. arXiv: 0902.0885.
- [5] PHOTONIS USA Pennsylvania Inc., 1000 New Holland Avenue, Lancaster, PA 17601-5688, USA.
- [6] Advanced Laser Diode Systems A.L.S. GmbH Schwarzschildstraße 6, 12489 Berlin, Germany.
- [7] LEO, W. R. *Techniques for Nuclear and Particle Physics Experiments: A How-to Approach*. Springer Berlin Heidelberg, 1994.